Cosmic evolution of star-forming galaxies to $z \simeq 1.8$ in the faint low-frequency radio source population

E. F. Ocran [1,2,3]★ A. R. Taylor,[1,2,3]★ M. Vaccari [2,3,4]★ C. H. Ishwara-Chandra,[3,5]
I. Prandoni [4], M. Prescott [2,3] and C. Mancuso[4]

[1]*Department of Astronomy, University of Cape Town, Private Bag X3, Rondebosch 7701, South Africa*
[2]*Department of Physics and Astronomy, University of the Western Cape, Private Bag X17, Bellville 7535, South Africa*
[3]*Inter-University Institute for Data Intensive Astronomy, Private Bag X3, Rondebosch 7701, South Africa*
[4]*INAF - Istituto di Radioastronomia, via Gobetti 101, I-40129 Bologna, Italy*
[5]*National Centre for Radio Astrophysics, Tata Institute of Fundamental Research, Pune 411007, India*

ABSTRACT

We study the properties of star-forming galaxies selected at 610 MHz with the GMRT in a survey covering $\sim$1.86 deg^2 down to a noise of $\sim$7.1 μJy beam^{-1}. These were identified by combining multiple classification diagnostics: optical, X-ray, infrared, and radio data. Of the 1685 SFGs from the GMRT sample, 496 have spectroscopic redshifts whereas 1189 have photometric redshifts. We find that the IRRC of star-forming galaxies, quantified by the infrared-to-1.4 GHz radio luminosity ratio q_{IR}, decreases with increasing redshift: $q_{\mathrm{IR}} = 2.86 \pm 0.04(1 + z)^{-0.20\pm0.02}$ out to $z \sim 1.8$. We use the V/V_{max} statistic to quantify the evolution of the comoving space density of the SFG sample. Averaged over luminosity our results indicate $\langle V/V_{\mathrm{max}} \rangle$ to be 0.51 ± 0.06, which is consistent with no evolution in overall space density. However, we find V/V_{max} to be a function of radio luminosity, indicating strong luminosity evolution with redshift. We explore the evolution of the SFGs radio luminosity function by separating the source into five redshift bins and comparing to theoretical model predictions. We find a strong redshift trend that can be fitted with a pure luminosity evolution of the form $L_{610\,\mathrm{MHz}} \propto (1 + z)^{(2.95\pm0.19)-(0.50\pm0.15)z}$. We calculate the cosmic SFR density since $z \sim 1.5$ by integrating the parametric fits of the evolved 610 MHz luminosity function. Our sample reproduces the expected steep decline in the star formation rate density since $z \sim 1$.

Key words: galaxies: luminosity function – galaxies: starburst – large-scale structure of Universe – radio continuum: galaxies.

1 INTRODUCTION

Radio continuum observations provide dust-unbiased information on mechanical feedback originating in star formation and active galactic nucleus (AGN) radio jets (Condon 1992; Merloni & Heinz 2007; Madau & Dickinson 2014). They thus underpin our understanding of galaxy evolution over cosmic time. Multiwavelength analysis of the Giant Metrewave Radio Telescope (GMRT) 610 MHz deep ELAIS-N1 data down to flux densities of 50 μJy by Ocran et al. (2017) clearly shows the transition from an AGN-dominated population to a star-forming galaxy (SFG) below flux densities of $\sim$ 300 μJy . This is in line with what found in 1.4 GHz deep surveys. This flux depends on the frequency (Condon 1989; Mauch & Sadler 2007; Padovani et al. 2015; Prandoni et al. 2018).

The synchrotron emission in SFGs is closely related to recent star formation, so that its emission is widely used as a star formation indicator. This is due to the short lifetime of the massive stars producing Type II and Type Ib supernovae (e.g. see Condon 1992; Bell 2003; Murphy et al. 2011a). The total infrared luminosity of a galaxy and its total 1.4 GHz radio luminosity are known to be linearly and tightly correlated (e.g. see van der Kruit 1971; de Jong et al. 1985; Helou, Soifer & Rowan-Robinson 1985; Condon 1992; Bell 2003; Sargent et al. 2010). This so-called infrared–radio correlation (IRRC) is well established for SFGs (e.g. Ivison et al. 2010; Magnelli et al. 2010; Thomson et al. 2014).

The evolution of different radio populations conducted by using non-parametric V/V_{max} statistic (Schmidt 1968; Morris et al. 1991; Yun, Reddy & Condon 2001). Clewley & Jarvis (2004) used the V/V_{max} test to show that low-luminosity radio sources evolve differently from their more powerful, predominantly Fanaroff-Riley type II (FRII). McAlpine & Jarvis (2011)

★ E-mail: ocran62@gmail.com (EFO); russ@ast.uct.ac.za (ART); mattia.vaccari@gmail.com (MV)

used V/V_{max} test to investigate the cosmic evolution of low-luminosity ($L_{1.4}$GHz $< 10^{25}$ W Hz^{-1}sr^{-1}) radio sources in the XMM Large-Scale Structure survey field (XMM-LSS). Their results indicate that the low-luminosity sources evolve differently to their high-luminosity counterparts out to a redshift of $z \sim 0.8$.

The bivariate luminosity function of an optical-radio matches sample describes the volume density of galaxies per unit interval of radio luminosity per interval of optical luminosity in each redshift bin. The evolution of SFGs has been extensively studied over the years using optical and infrared surveys. Mid- and far-infrared (FIR) *Spitzer* observations indicate that the galaxy population undergoes pure luminosity evolution with $k_D \sim 3.4-3.8$ out to $z \sim 1.2$, where k_D is the pure density evolution (PDE; e.g. Caputi et al. 2007; Magnelli et al. 2009; Rujopakarn et al. 2010; Magnelli et al. 2011). While FIR luminosity functions from Herschel data result in slightly stronger evolution estimates with $L_\star \propto (1 + z)^{4.1 \pm 0.3}$ up to $z \sim 1.5$ (Gruppioni et al. 2010; Lapi et al. 2011). At low redshifts ($z < 0.5$), Herschel studies performed by Dye et al. (2010) suggested evidence of stronger evolution in SFGs with the total luminosity density evolving as $(1 + z)^{7.1}$.

At radio wavelengths there has been substantial work on AGNs but SFGs only become significant at low flux densities, hence are becoming more accessible with deep surveys. Mauch & Sadler (2007) studied a sample of 7824 radio sources from 1.4 GHz NRAO Very Large Array (VLA) Sky Survey (NVSS) with galaxies brighter than $K = 12.75$ mag in the Second Incremental Data Release of 6dF Galaxy Survey (6dFGSDR2) that spanned a redshift range $0.003 < z < 0.3$ and determined the local luminosity function at 1.4 GHz for their 60 per cent SFGs and 40 per cent AGNs. Smolčić et al. (2009a) derived the cosmic star formation history (CSFH) out to $z = 1.3$ using a sample of ~ 350 radio-selected SFGs and determined an evolution in the 1.4 GHz luminosity function based on the VLA-COSMOS SFGs. Mao et al. (2012) used the Data Release 1 (DR1) from the Australia Telescope Large Area Survey consisting of the preliminary data published by Norris et al. (2006) and Middelberg et al. (2008) and reaching an rms sensitivity of 30 μJy beam^{-1} to derive radio luminosity functions (RLFs). They constructed the RLF for SFGs to $z = 0.5$ and for AGNs to $z = 0.8$ and found that RLF for SFGs appears to be in good agreement with previous studies. McAlpine, Jarvis & Bonfield (2013) investigated the evolution of faint radio sources out to $z \sim 2.5$ by combining a 1 square degree VLA radio survey complete to a depth of 100 μJy with the following surveys: Visible and Infrared Survey Telescope for Astronomy Deep Extragalactic Observations and Canadian–France–Hawaii Telescope Legacy Survey. Novak et al. (2017) use of the deep Karl G. Jansky Very Large Array (VLA) COSMOS radio observations at 3 GHz to infer RLFs of SFGs up to redshift of $z \sim 5$ based on 6040 detections with reliable optical counterparts.

In the low-frequency regime, Willott et al. (2001) measure the RLF of steep-spectrum radio sources using three redshift surveys of flux-limited samples selected at low (151 and 178 MHz) radio frequency, low-frequency source counts, and the local RLF. Prescott et al. (2016) presented a measurement of the evolution of SFGs to $z = 0.5$, by matching a catalogue of radio sources measured at a frequency of 325 MHz from the GMRT to their optical counterparts in the Galaxy And Mass Assembly survey. They found that the radio RLF at 325 MHz for SFGs closely follows that measured at 1.4 GHz.

The evolution of the global galaxy SFR density can be used as a robust constraint on various simulations and semi-analytic models of galaxy evolution (e.g. Pei, Fall & Hauser 1999; McCarthy et al. 2001; Somerville et al. 2001). Total CSFH has been constrained using MIR (24/8 μm) selected samples obtained by deep small area surveys (Zheng et al. 2006; Bell et al. 2007; Caputi et al. 2007). Smolčić et al. (2009a) used the VLA-COSMOS SFGs to derive the CSFH out to $z = 1.3$. In this paper, we present a measurement of the evolution of SF galaxies to $z \sim 1.5$, by matching a catalogue of radio sources measured at a frequency of 610 MHz from the GMRT to their optical counterparts in the SERVS Data Fusion[1] (Vaccari et al. 2010; Vaccari 2015). The 610 MHz GMRT survey covers a sky area of ~ 1.86 deg^2. The restoring beam is 6 arcsec circular and the RMS in the central region is ~ 7.1 μJy beam^{-1} making this survey the most sensitive low-frequency deep field to date. The SERVS Data Fusion provides reliable spectroscopic and photometric redshifts, allowing us to classify AGNs and SFGs. The layout of this paper is as follows: we first introduce the 610 MHz SFG data in Section 2. In Section 3, we present the sample properties of the selected SFGs. The estimation of the RLF is discussed in Section 4. In Section 5, we describe how we constrain the evolution of the SFG luminosity function out to $z \simeq 1.5$. The implications for the cosmic star formation density are presented in Section 6. We adopt throughout the paper a flat concordance Lambda cold dark matter, with the following parameters: Hubble constant H$_0 = 70$ km s^{-1} Mpc^{-1}, dark energy density $\Omega_\Lambda = 0.7$, and matter density $\Omega_m = 0.3$.

2 THE 610 MHz GMRT DATA

The radio data we use in this paper is taken from the GMRT at 610 MHz covering ~ 1.86 deg^2 of EN1 field. The survey consisted of seven closely spaced pointings. The on-source integration time was ~ 18 h per pointing. The resolutions before mosaic for each pointing were in the range 4.5 to 6 arcsec. The minimum rms noise in the central region of the image is 7.1 μJy beam^{-1}. The radio data are fully described in Ocran et al. (2019). Data analysis was carried out on the data-intensive cloud at the Inter-University Institute for Data Intensive Astronomy. A source catalogue was produced by extracting sources in the mosaic using the PYBDSF source finder (Mohan & Rafferty 2015). This resulted in a final catalogue of 4290 radio sources. By matching to multiwavelength data against SERVS IRAC12 positions Fusion[2] (Vaccari et al. 2010; Vaccari 2015), we obtain a redshift estimate for 72 per cent, with 19 per cent based on spectroscopy. The redshift estimates are a combination of spectroscopic and photometric redshifts from the Hyper Suprime-Cam (HSC) Photometric Redshift Catalogue (Tanaka et al. 2018), the revised SWIRE Photometric Redshift Catalogue (Rowan-Robinson et al. 2013), and the Herschel Extragalactic Legacy Project (HELP; Vaccari 2016; Shirley et al. 2019). For 3105 of the sources with redshifts, we use radio and X-ray luminosity, optical line ratios, mid-infrared colours, and 24 μm and IR-to-radio flux ratios to separate SFGs from AGNs. In Ocran et al. (2019), we outlined that total number of sources with redshifts for which we can define at least one AGN indicator was 2305 (i.e. $\sim$ 54 per cent of the whole 4290 sample and $\sim$ 74 per cent of the 3105 sources with redshifts). We classified 1685 sources as SFG constituting 73 per cent of the

---

[1] http://www.mattiavaccari.net/df
[2] http://www.mattiavaccari.net/df

2305 sources for which we were able to define at least one AGN indicator for source classification. For sources with redshift, rest frame 610 MHz radio luminosities are calculated using equation (1) as

$$L_{610} = 4\pi D_{\mathrm{L}}^2 \frac{S_{\mathrm{obs}}}{(1+z)^{1+\alpha}}, \tag{1}$$

where L is the luminosity in $\mathrm{W\,Hz^{-1}}$ at the frequency ν, D_{L} is the luminosity distance in metres. S_{obs} is the observed flux density at 610 MHz, and α is the spectral index and it is defined as $S \propto \nu^\alpha$. In Ocran et al. (2019), we measured a median spectral index that steepens with frequency with $\alpha_{325}^{610} = -0.80 \pm 0.29$, for ~479 sources and $\alpha_{1400}^{610} = -0.83 \pm 0.31$ for ~99 sources. Hence, we use the canonical spectral index of $\alpha = -0.8$ often assumed for SFGs (Condon 1992).

2.1 The SFG sample

From Ocran et al. (2019), we have a multiwavelength match for 92 per cent of the sources and a redshift identification for 72 per cent of the sources. But we have been able to classify 39 per cent as SFGs and 15 per cent as AGNs which adds up to 54 per cent. If there is an indication of AGN activity in the source from any of the criteria adopted, then we inferred that the source is an AGN, regardless of the results from the other indicators. Thus, the sources classified as SFGs are those sources in our redshift sample that do not show evidence of AGN activity in any of the diagnostics. This may be considered as an upper limit to the population of sources in this flux density regime whose radio emission is powered by star formation processes.

Fig. 1 shows the distribution of 610-MHz flux densities. The entire GMRT sample of 4290 sources (i.e. light grey histogram) is represented as S_{ALL}. Radio sources that have multiwavelength identification (i.e. black histogram) are represented as S_{matched}, whereas radio sources with redshifts (i.e. red histogram) are represented S_z. The sources with redshifts that also have at least one diagnostic for AGN activity (i.e. this sample is fully described in Ocran et al. 2019 and Section 2, see blue histogram) are represented as $S_{\mathrm{AGN\,diagnostic}}$. The SFG sample used for this analysis is drawn from the latter. We use these distributions to derive the redshift success C_z completeness which is outlined in Subsection 4.2.
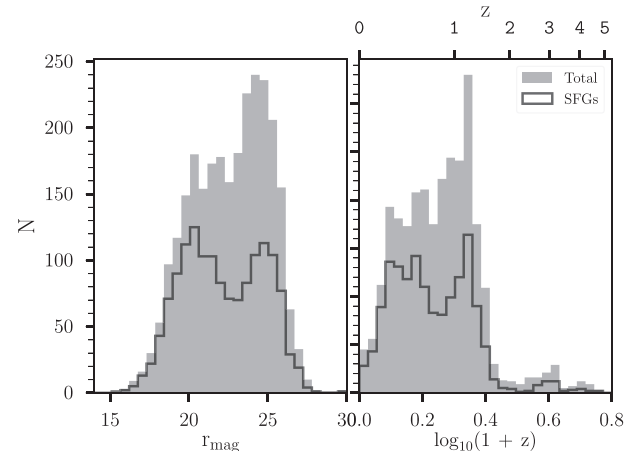
3 SFG PROPERTIES

Fig. 2 shows the distribution of the GMRT sources (grey histogram) with r_{mag} (left) and redshift (right). We overplot the distribution of objects identified as SFG in black. The redshift distribution clearly shows that the sample is incomplete for $r_{\mathrm{mag}} > 25$ and $z > 1.5$. This is driven by HSC/Subaru photometric redshifts, which start being incomplete at $z \sim 1.3$. Tanaka et al. (2018) stress that photometric redshifts should only be used at $z \lesssim 1.5$ and $i \lesssim 25$.

We note a secondary peak in our sample at $z \sim 1.1$ and $r \sim 25$. Swinbank et al. (2007) identified five candidate galaxy over densities at $z \sim 1$ across $\sim 1\,\mathrm{deg}^2$ in the EN1 field by analysing deep field of the UK Infrared Deep Sky Survey (UKIDSS) Deep eXtragalactic Survey. They attributed these five overdense regions lying in a narrow redshift range as an indication of the presence of a supercluster in this field at $z \sim 1$. Our secondary peak may be due to this supercluster.
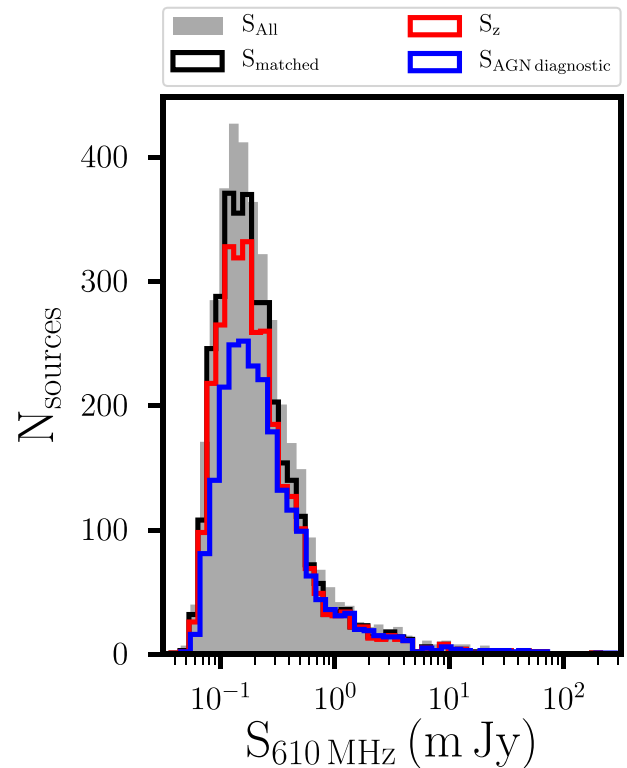
Figure 1. The distribution of 610-MHz flux densities for the entire GMRT sample of 4290 sources (light grey), radio sources that have multiwavelength identification (black), radio sources with redshifts (red), and sources with redshifts that also have at least one diagnostic for AGN activity (blue).


Figure 2. Distribution of the GMRT sources (grey histogram) with r_{mag} (left) and redshift (right). The distribution of SFG (black) are overplotted in both panels.

3.1 The redshift evolution of the IRRC

We characterized the IRRC of our SFGs by the logarithmic ratio between the IR bolometric (8–1000 μm) luminosity and the radio luminosity q_{IR} (Helou et al. 1985).

$$q_{\mathrm{IR}} = \log_{10}\left(\frac{L_{\mathrm{IR}}}{3.75 \times 10^{12}\,\mathrm{W}}\right) - \log_{10}\left(\frac{L_{\mathrm{radio}}}{\mathrm{W\,Hz^{-1}}}\right), \tag{2}$$

where L_{IR} is the total rest-frame infrared luminosity and L_{radio} is the luminosity at the radio frequency to be studied, in our case
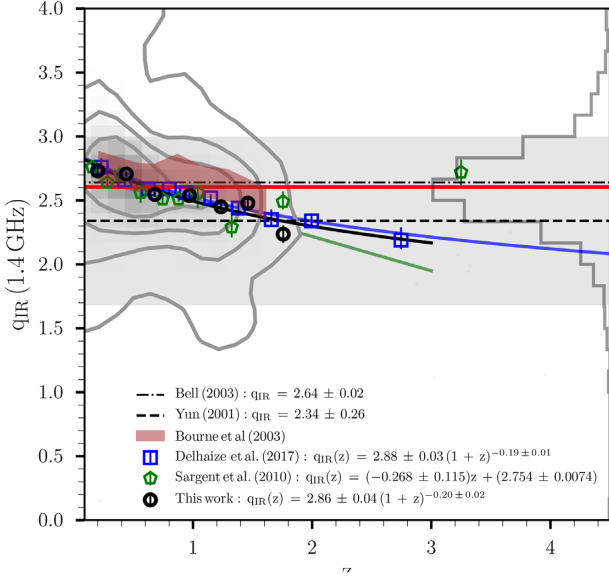
Figure 3. The q_{IR} versus redshift for SFGs. The background grey density contour represents the q_{IR} for SFGs with radio and IR detection, and redshift information. The contours levels are 1, 2, 3, and 4σ. The inset histogram represents the q_{IR} distribution. The median q_{IR} within each redshift bin is indicated by the open black circle. The error bars show the 1σ dispersion calculated via bootstrap method. The solid black line shows the power-law fit to the our SFGs sample. The horizontal shaded region represents the ±0.26 upper and lower bounds around the median value of Yun et al. (2001).

Table 1. The number of sources, median value of z, and q_{IR} for SFGs in each redshift bin.

z	Median(z)	q_{IR}(1.4 GHz)
0.002−0.282	0.20	2.73 ± 0.03
0.282−0.562	0.44	2.71 ± 0.02
0.562−0.842	0.68	2.57 ± 0.02
0.842−1.122	0.97	2.54 ± 0.02
1.122−1.402	1.23	2.45 ± 0.03
1.402−1.682	1.46	2.48 ± 0.04
1.682−1.962	1.80	2.24 ± 0.07

fitting a power-law function to the median values of q_{IR}, weighting by the uncertainty, we find a significant variation of q_{IR} with redshift: $q_{IR} = 2.86 \pm 0.04(1 + z)^{-0.20\pm0.02}$. The errors here are the 1σ uncertainty from the power-law fit. Our result is in good agreement with Delhaize et al. (2017), who carried out double-censored survival analysis (following Sargent et al. 2010) to calculate the median q_{IR} values (and associated 95 per cent confidence intervals) for their samples in redshift bins. To get q_{IR} they converted their 3 GHz luminosities to 1.4 GHz ones using a spectral index of 0.7. They reported a slightly higher but statistically significant variation of q_{IR} with redshift: $q_{IR} = 2.88 \pm 0.03(1 + z)^{-0.19\pm0.01}$ from a highly sensitive 3 GHz observations with the Karl G. Jansky Very Large Array (VLA) and infrared data from the Herschel Space Observatory in the 2 deg^2 COSMOS field. Despite the fact that we do not follow the survival analysis approach (see Schmitt et al. 1993; Novak et al. 2017; Ceraj et al. 2018; Molnár et al. 2018), we nevertheless get results in good agreement, implying that our analysis is not significantly biased.

Magnelli et al. (2015) found a moderate but statistically significant redshift evolution $q_{IR}(z) = 2.35 \pm 0.08(1 + z)^{-0.12\pm0.04}$ using deep FIR luminosities from the *Herschel* Space Observatory (Pilbratt et al. 2010) and deep radio 1.4 GHz VLA observations. Calistro Rivera et al. (2017) measured the redshift evolution of the IRRC for SFG sample obtained with Low Frequency Array (LOFAR) at 150 MHz and found that the ratio of total infrared to 1.4 GHz data of the Bootes field decreases with increasing redshift given by $q_{IR} = 2.45 \pm 0.04(1 + z)^{-0.15\pm0.03}$.

Under our assumption of a fixed spectral index $\alpha = -0.8$, q_{IR} (610 MHz) is given by the simple conversion $q_{610\,MHz} = q_{1.4GHz} - 0.29$. We thus report a median q_{IR} (610 MHz) = 2.32, and $q_{610\,MHz} = 2.57 \pm 0.04(1 + z)^{-0.120\pm0.02}$ as a function of redshift.

4 RADIO LUMINOSITY FUNCTION

4.1 Sample selection

To study the evolution of the RLF, we limit our sample to SFGs with r_{mag} lim = 25 and $0.002 < z < 1.5$, making 1291 SFGs in total. We choose r_{mag} lim = 25 to maximize the number of sources that we can use to calculate the luminosity function. Table 2 presents a summary of the number and percentage of all the SFGs with spectroscopic and photometric redshifts (a). The number and percentage of the SFGs that satisfy the selection for computing the luminosity function (b). The r_{mag} versus redshift for the SFG sample with redshift estimates and r_{mag} limit of 25 (see the dashed horizontal red line) is plotted in the left-hand panel of Fig. 4. The right-hand panel of this plot shows the 610 MHz luminosity versus

at 610 MHz and 1.4 GHz in W/Hz. The 1.4 GHz luminosities were computed from the $S_{610\,MHz}$ using a radio spectral index of -0.8. The FIR luminosities, L_{IR}, were derived from rest-frame-integrated 8–1000 µm luminosities, estimated by Małek et al. (2018) using HELP photometry. They were obtained by performing SED fitting on the ultraviolet (UV)/near-infrared (NIR) to FIR emission of 42 047 galaxies from the pilot HELP field: EN1. We corrected the luminosity values to our more accurate spectroscopic redshift by following the prescription presented by Ocran et al. (2017).

We investigate the evolution of the q_{IR} parameter with redshift which is quantified by the function $q_{IR} \propto (1 + z)^\gamma$ (Ivison et al. 2010; Calistro Rivera et al. 2017). We first analyse the 1.4 GHz behaviour because this can be compared to the literature. Fig. 3 shows q_{IR} versus redshift. The inset histogram shows q_{IR} is scattered in a distribution with an overall median value of $q_{IR} = 2.61^{+0.30}_{-0.28}$ (see the red horizontal solid line in Fig. 3). This q_{IR} distribution agrees well with previous literature within the errors. Yun et al. (2001) measured a median $q_{IR} = 2.34 \pm 0.26$ (see the dashed horizontal line in Fig. 3), by investigating the radio counterparts to the IRAS redshift survey galaxies that are also identified in the NRAO VLA Sky Survey (NVSS) catalogue. The horizontal shaded region represents the ±0.26 upper and lower bounds around the median value. Bell (2003) assembled a diverse sample of galaxies from the literature with far-ultraviolet (FUV), optical, infrared (IR), and radio luminosities to explore the origin of the IRRC and measured a median $q_{IR} = 2.64 \pm 0.02$ (see the dot–dashed horizontal line in Fig. 3). We note that Bell (2003) used total infrared luminosities, but Yun et al. (2001) value is based on FIR luminosities. Delhaize et al. (2017) showed that this usually results in lower median values. We split the data into seven redshift bins; Table 1 presents the number of sources, median value of z, and q_{IR} for SFGs in each redshift bin. By

Table 2. Summary of the number and percentage of all the SFGs with spectroscopic and photometric redshifts (a). The number and percentage of the SFGs that satisfy the selection for computing the luminosity function (b).

	Number	Percentage
(a) All SFGs (1685 sources).		
z_{phot}	1189	70.5
z_{spec}	496	29.5
(b) SFGs and selection criteria (1291 sources,		
i.e. SFGs $\wedge$ $r = 25$ $\wedge$ $0.002 < z < 1.5$).		
z_{phot}	834	64.6
z_{spec}	457	35.4

Notes. z_{phot} – photometric redshift.

z_{spec} – spectroscopic redshift.
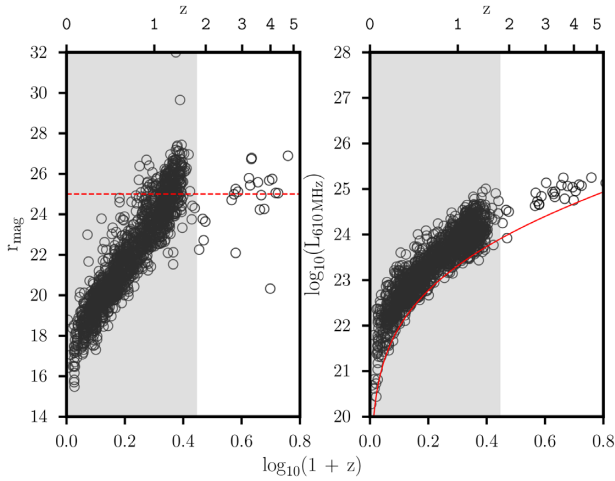
Figure 4. r_{mag} versus redshift for the SFG sample with redshift estimates and r_{mag} limit of 25 (the dashed horizontal red line) (left-hand panel). 610 MHz luminosity versus redshift for the GMRT SFG (open black circles) sample with redshift and r_{mag} limit of 25 (right-hand panel). The luminosity limit implied by the GMRT sensitivity is shown by the solid red curve.

redshift for the GMRT sample with redshift and limiting magnitude of $r = 25$.

4.2 V/V_{max} statistic

In order to assess the evolution in the comoving space density of radio sources, we use the non-parametric V/V_{max} method (Rowan-Robinson 1968; Schmidt 1968). V_{max} is the volume over which the galaxy could have been observed given the selection limits. It allows the incorporation of additional selection criteria.

For a uniform distribution, the value of V/V_{max} will be uniformly distributed between 0 and 1. Thus, for such a sample the mean value is $\langle (V/V_{max}) \rangle = 0.5 \pm (12N)^{-1/2}$, where N is the number of objects in the sample. $\langle (V/V_{max}) \rangle > 0.5$ indicates that the sources are biased towards larger distances, or an increase of the space density with redshift. $\langle (V/V_{max}) \rangle < 0.5$ indicates a deficiency in high-redshift sources, or a decline in the space density with redshift. A constant comoving population is given by $\langle (V/V_{max}) \rangle = 0.5$ (Clewley & Jarvis 2004; Tasse et al. 2008; McAlpine & Jarvis 2011; McAlpine et al. 2013; Prescott et al. 2016).

Our sample is a matched radio/optical sample, thus we take into account both the optical and radio limits of the surveys, where V_{max}, the final maximum observable volume, is taken as the minimum from the optical and radio V_{max} for each source:

$$V_{max} = \min(V_{max,radio}, V_{max,optical}), \qquad (3)$$

where $V_{max,radio}$ and $V_{max,optical}$ represent the maximum observable volumes of the source in the radio and optical surveys, respectively, and are shown below:

$$V_{max,radio} = \sum_{i=1}^{n} V_{max,radio,i}(z_{max,radio,i}) \times \mathcal{C}_i \qquad (4)$$

$$V_{max,optical} = \sum_{i=1}^{n} V_{max,optical,i}(z_{max,optical,i}) \times \mathcal{C}_i. \qquad (5)$$

$V_{max,radio}$ and $V_{max,optical}$ were computed from $z_{max,radio}$ and $z_{max,optical}$ as shown in equations (4) and (5) above. This is in a single redshift bin and that the sum goes over all galaxies in a given redshift bin. The $z_{max,radio}$ and $z_{max,optical}$ represent the maximum observable redshifts of the source in the radio and optical surveys, respectively. The k-correction to the $V_{max,radio}$ is a power law. We estimate $z_{max,optical}$ by running `kcorrect` (Blanton et al. 2003) which redshifts the best-fitting SED template from the photometric redshift estimation procedure and determine the redshift where the template becomes fainter than our imposed limiting magnitude of $r = 25$. The derivation of the radio completeness C_f is given by $\epsilon(s)$ (see Ocran et al. 2019). The $\epsilon(s)$ is the probability that a source with true flux density, s, will result in a detection. We measured this by inserting 3000 artificial point sources at a given true flux density at random positions into the residual map with the original sources removed. These sources populate the image with the same background noise and rms properties as the original source finding. We stressed in Ocran et al. (2019) that the field-of-view effect dominates the curve in the radio completeness correction (see fig. 7, Ocran et al. 2019) since the analysis is incorporating the varying sensitivity limit across the field of view due to the GMRT primary beam. This represents the completeness of the radio source catalogue versus true flux density (see Ocran et al. 2019). In order to correct for the redshift incompleteness, we divided the distribution for the entire sample (i.e. light grey histogram, see Fig. 2) by the distribution for the sources with at least one diagnostic for AGN activity (i.e. blue histogram). We then corrected the RLF with this redshift success completeness, C_z. This redshift incompleteness in our sample is mostly due to sources not being detected in the optical wavelength range, so that we cannot compute a reliable (photometric) redshift. We define the completeness correction factor $\mathcal{C}_i$ (i.e. see equations 4 and 5) as

$$\mathcal{C} = C_z \times C_f. \qquad (6)$$

C_z is the redshift success completeness and C_f is the completeness of the radio catalogue.

In Fig. 5 and Table 3, we show the mean V/V_{max} statistic in bins of radio luminosity in the range $10^{20} < L_{610MHz} < 10^{25}$ WHz^{-1} for our SFG sample (see open black circles). For each bin, we provide the number of sources (N) in the bin, mean $\langle V/V_{max} \rangle$, mean redshift ($\langle z \rangle$). The $\sigma = 1/\sqrt{12N}$ (Avni & Bahcall 1980) are the statistical errors derived from the sample size. The dashed horizontal line shows the median $\langle V/V_{max} \rangle$. We calculate $\langle V/V_{max} \rangle$ to be 0.51 ± 0.06 for our SFGs. This value is not significantly different from 0.5, given the error of 0.06 thus averaged over luminosity there is no overall evidence for evolution in the number density of SFGs. However, there is a clear trend of V/V_{max} with radio
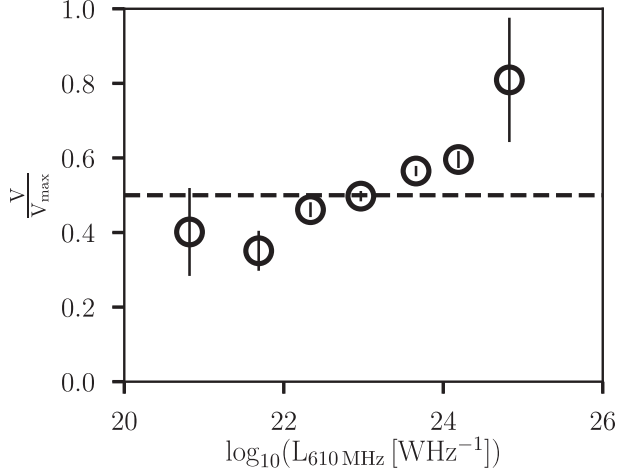
Figure 5. The V/V_{max} statistic as a function the radio luminosity for SFG out to $z = 1.5$ for the GMRT data (open black circles).

Table 3. The V/V_{max} statistic as in radio luminosity bins for SFGs.

Median luminosity $\log_{10}(L_{610\,MHz}\,[WHz^{-1}])$	Number (SFG)	V/V_{max} (SFG)	$1/\sqrt{12N}$ (SFG)
20.82	6	0.446	0.12
21.72	29	0.258	0.05
22.34	211	0.456	0.02
22.97	433	0.494	0.01
23.66	442	0.569	0.01
24.33	162	0.583	0.02
24.93	3	0.729	0.17

luminosity. At faint radio luminosities $L_{610MHz} < 10^{23}$ WHz^{-1} the values are below 0.5 indicating a higher space density at low redshift. Conversely, for high luminosity ($L_{610MHz} > 10^{23}$ WHz^{-1}) there is evidence for positive evolution or higher space density at higher redshift. The strong evolution of the high-luminosity radio sources was also detected by Clewley & Jarvis (2004). McAlpine & Jarvis (2011) also found evidence of this strong evolution at high luminosities although their result is at a lower statistical significance due to the small size of their sample. Taken together, the results indicate strong luminosity evolution with overall number density constant with redshift but more high-luminosity sources and fewer low-luminosity objects at higher redshift.

4.3 Derivation of the radio luminosity function

We derive the radio LF (Φ) for our GMRT sample in five redshift bins using the standard $\frac{1}{V_{max}}$ method (Schmidt 1968).

As the GMRT mosaics have non-uniform sensitivity, the effective area of the survey changes as a function of the flux limit. The volume of space available to a source of a given luminosity $V_{max,radio}$ (L) has to be calculated by taking into account the variation of survey area as a function of flux density limit. The RLF for a given luminosity bin is given by

$$\Phi_z(L) = \sum_{i=1}^{n} \frac{1}{V_{max,i}} \pm \sqrt{\sum_{i=1}^{n} \frac{1}{V_{max,i}^2}}, \qquad (7)$$

where $\Phi_z(L)$ is the density of sources in Mpc^{-3} dex^{-1}.
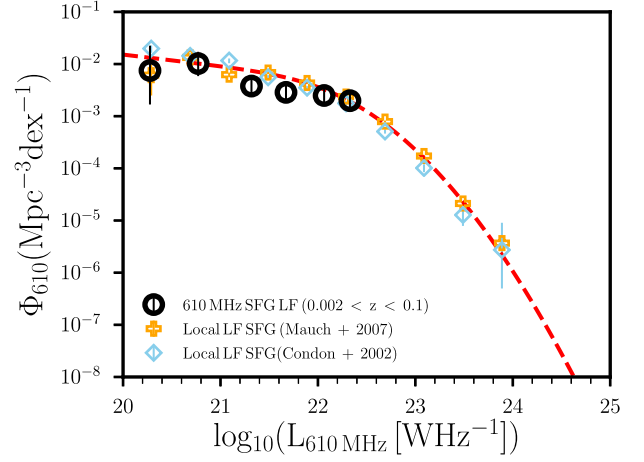
Figure 6. The local 610 MHz SFG luminosity function. The yellow plus and blue stars represent Mauch & Sadler (2007) and Condon et al. (2002) SFG volume densities scaled to 610 MHz using an $\alpha = -0.8$. The dashed red line is the combined analytic fit performed by Novak et al. (2017) to the local radio LF of SFGs from several surveys with different observed areas and sensitivities.

5 COSMIC EVOLUTION OF THE SFG RADIO LUMINOSITY FUNCTION

In this section, we explain the reasoning behind adopting the analytic form of our local luminosity function at 610 MHz to fit our data. We further describe how the evolution of SFG luminosity function out to $z \sim 1.5$ is constrained.

5.1 The local RLF

Fig. 6 presents the local 610 MHz SFG luminosity function shown as open black circles. The sample is truncated at $z < 0.1$ to minimize the effects of evolution. The yellow plus and blue stars represent Mauch & Sadler (2007) and Condon, Cotton & Broderick (2002) SFG volume densities scaled to 610 MHz using an $\alpha = -0.8$. The dashed red line is the analytic fit to the local 610 MHz SFG data. We also show the 610 MHz RLF for SFGs in the redshift range $0.002 < z < 1.5$ shown in open black circles in Fig. A1.

An analytic function of the type described by Saunders et al. (1990)

$$\Phi_o(L) = \Phi_\star \left(\frac{L}{L_\star}\right)^{1-\alpha} \exp\left[\frac{-1}{2\sigma^2} \log^2\left(1 + \frac{L}{L_\star}\right)\right], \qquad (8)$$

where the $L_\star$ parameter describes the position of the turnover of the power-law plus lognormal distribution, $\Phi_\star$ is the normalization, α and σ are the faint and bright ends of the distribution, respectively.

To obtain the analytic form of the local luminosity function that is used throughout this work, we use the best-fitting parameters from Novak et al. (2017), who combined data from both wide and deep surveys to properly constrain both the faint and the bright end of the local LF form Condon et al. (2002), Best et al. (2005), Mauch & Sadler (2007) data using the form given in equation (8). The best-fitting parameters obtained by Novak et al. (2017), which we use throughout this work are $\Phi_\star = 3.55 \times 10^3$ Mpc^{-3} dex^{-1}, $L_\star = 1.85 \times 10^{21}$ WHz^{-1}, $\alpha = 1.22$, $\sigma = 0.63$.

Table 4. Luminosity functions of SFG obtained with the $1/V_{max}$ method for different redshift bins.

Redshift z	Luminosity $\log_{10}(L_{610\,MHz}\,[\mathrm{WHz^{-1}}])$	Number density $\Phi_{610}(\mathrm{Mpc^{-3}\,dex^{-1}})$	Number N
$0.002 < z < 0.25$	20.28	$7.51^{+14.64}_{-5.70} \times 10^{-3}$	1
	20.77	$1.02^{+14.64}_{-5.70} \times 10^{-2}$	4
	21.32	$3.25^{+14.64}_{-5.70} \times 10^{-3}$	6
	21.67	$2.63^{+14.64}_{-5.70} \times 10^{-3}$	20
	22.10	$3.68^{+14.64}_{-5.70} \times 10^{-3}$	68
	22.36	$2.53^{+14.64}_{-5.70} \times 10^{-3}$	89
	22.74	$7.21^{+14.64}_{-5.70} \times 10^{-4}$	36
	23.21	$9.81^{+14.64}_{-5.70} \times 10^{-5}$	5
$0.25 < z < 0.5$	22.50	$1.86^{+0.24}_{-0.21} \times 10^{-3}$	58
	22.80	$1.69^{+0.16}_{-0.11} \times 10^{-3}$	176
	23.14	$5.01^{+0.44}_{-0.40} \times 10^{-4}$	113
	23.51	$5.63^{+1.53}_{-1.21} \times 10^{-5}$	16
	23.93	$6.98^{+7.95}_{-4.10} \times 10^{-6}$	2
$0.5 < z < 0.9$	23.23	$5.75^{+0.46}_{-0.42} \times 10^{-4}$	135
	23.57	$2.51^{+0.18}_{-0.17} \times 10^{-4}$	163
	23.94	$4.17^{+0.63}_{-0.54} \times 10^{-5}$	43
	24.24	$8.99^{+17.93}_{-6.98} \times 10^{-7}$	1
$0.9 < z < 1.2$	23.68	$2.64^{+0.30}_{-0.27} \times 10^{-4}$	71
	23.96	$1.39^{+0.12}_{-0.11} \times 10^{-4}$	117
	24.31	$3.89^{+0.54}_{-0.47} \times 10^{-5}$	49
	24.65	$7.81^{+0.16}_{-6.07} \times 10^{-7}$	1
$1.2 < z < 1.5$	23.98	$9.46^{+1.35}_{-1.18} \times 10^{-5}$	47
	24.37	$1.85^{+0.39}_{-0.32} \times 10^{-5}$	24
	24.67	$3.25^{+1.89}_{-1.24} \times 10^{-6}$	5
	25.00	$6.44^{+12.84}_{-5.00} \times 10^{-7}$	2

Note. The listed luminosity values represent the median luminosity of the sources in the corresponding luminosity bin.

Table 5. Best-fitting evolution parameters obtained by the fitting local luminosity function to the redshift binned data assuming pure luminosity k_L evolution and the SFRD derived.

Med(z)	k_L	Total	Lower limits
		SFRD [$\mathrm{M_\odot\,yr^{-1}\,Mpc^{-3}}$]	
$0.18^{+0.05}_{-0.07}$	2.88 ± 0.48	$0.021^{+0.004}_{-0.003}$	$0.014^{0.004}_{0.002}$
$0.39^{+0.09}_{-0.10}$	2.89 ± 0.49	$0.026^{+0.004}_{-0.005}$	$0.018^{0.003}_{0.004}$
$0.66^{+0.16}_{-0.05}$	2.77 ± 0.46	$0.035^{+0.009}_{-0.005}$	$0.023^{0.009}_{0.005}$
$1.08^{+0.08}_{-0.13}$	2.67 ± 0.41	$0.046^{+0.006}_{-0.005}$	$0.016^{0.006}_{0.005}$
$1.28^{+0.13}_{-0.04}$	2.57 ± 0.40	$0.066^{+0.012}_{-0.007}$	$0.013^{0.007}_{0.002}$

5.2 RLF as a function of z

We compare our results with literature values of SFG LF derived at 1.4 GHz and scaled down to 610 MHz assuming $\alpha = -0.8$ to check the robustness of our LF. Fig. 7 presents the RLFs of SFGs at $\nu = 610\,\mathrm{MHz}$ in different redshift bins (black open circles). Scaled down luminosity functions from 1.4 GHz to 610 MHz by Smolčić et al. (2009a), McAlpine et al. (2013), and Novak et al. (2017) are shown as green pluses, orange pentagons, and blue diamonds, respectively, in each panel.

We compare with LFs derived from Wilman et al. (2008) semi-empirical simulation of the SKA and Mancuso et al. (2017) models. The Mancuso et al. (2017) models were obtained by following the model-independent approach by Mancuso et al. (2016a, b). These models are based on two main ingredients: (i) the redshift-dependent SFR functions inferred from the latest UV/far-IR data from *HST*/Herschel and related statistics of strong gravitationally lensed sources, and (ii) deterministic tracks for the co-evolution of star formation and BH accretion in an individual galaxy, determined from a wealth of multiwavelength observations (see Mancuso et al. 2017). We also compare to SFG models (see open brown diamonds in Fig. 7) from the Tiered Radio Extragalactic Continuum Simulation (T-RECS) by Bonaldi et al. (2019) who modelled the corresponding sub-populations, over the 150 MHz–20 GHz range. Our results concur with the results of these models from literature, especially to the Mancuso et al. (2017) and Bonaldi et al. (2019) models at high luminosities. Note, however, that in the first two redshift bins the faint end of the Mancuso et al. (2017) models is lower than that of our SFG LF. Also, the faint end of the Bonaldi et al. (2019) and Wilman et al. (2008) models are higher than our measured SFG LF.

The breakdown of the luminosity, number density ($\Phi_{610}(\mathrm{Mpc^{-3}\,dex^{-1}})$), and the number of sources in each redshift bin is presented in Table 4. Our data have small Poissonian error bars due to the relatively large number of sources in each bin and as such the errors do not reflect all possible systematic effects.

5.3 RLF evolution

Following Novak et al. (2017), we assume that the shape of the LF remains unchanged at all observed cosmic times and only allow the position of the turnover and the normalization to change with redshift. We used the Markov chain Monte Carlo (MCMC) algorithm module EMCEE (Foreman-Mackey et al. 2013), implemented in the LMFIT Python package (Newville et al. 2014), to perform a multivariate fit to the data. We fit all redshift slices for evolution assuming two scenarios for the LF, one in which the luminosity of
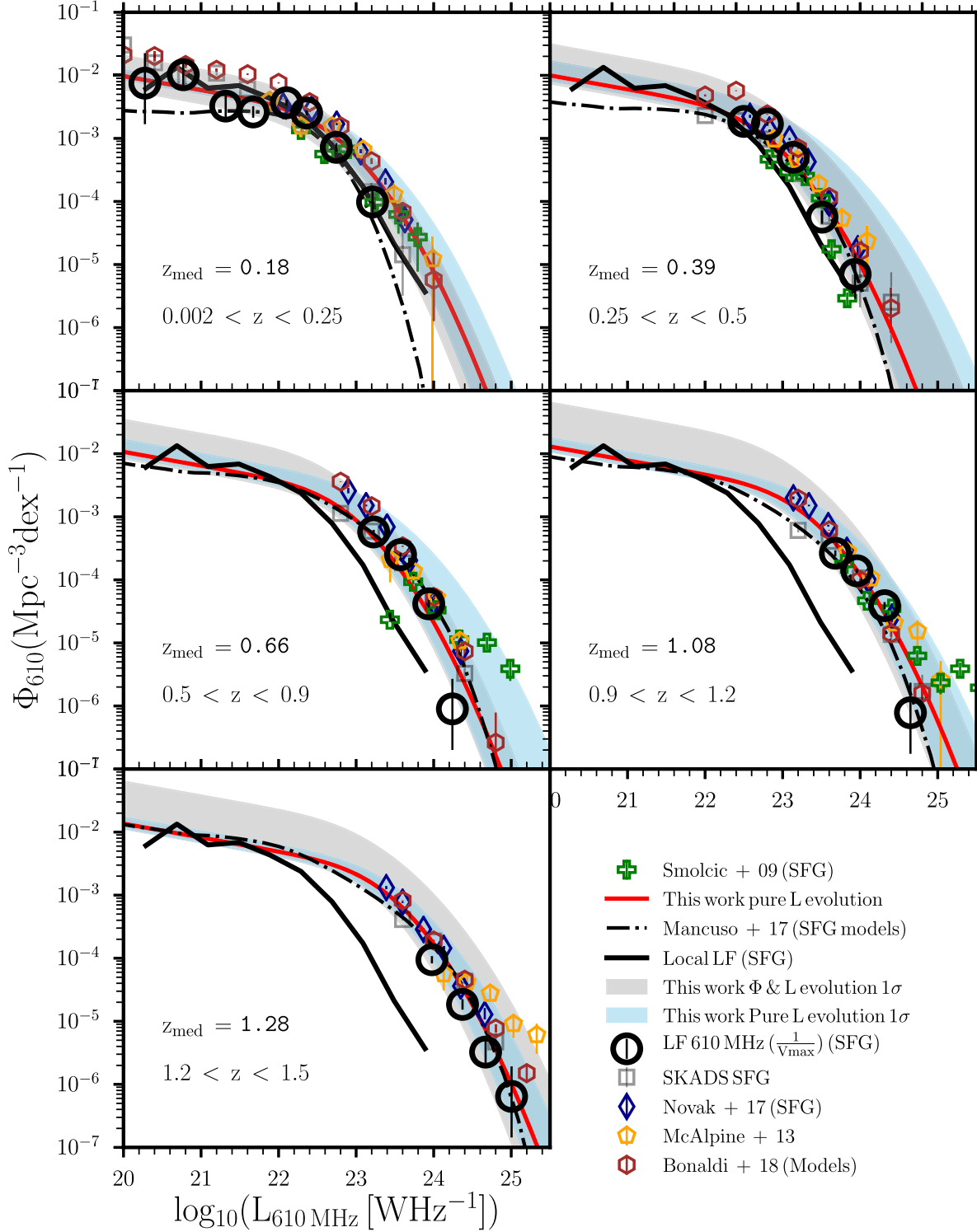
Figure 7. RLFs of SFGs at $\nu = 610\,\mathrm{MHz}$ in different redshift bins (black open circles). The black dashed lines in each panel are the SFG models from Mancuso et al. (2017). The black squares represent the total SFG LF from the semi-empirical simulation of the SKA (Wilman et al. 2008). Luminosity functions computed for SFGs from the T-RECS (Bonaldi et al. 2019) simulations are shown as open brown diamonds. The local RLF of Mauch & Sadler (2007) is shown for reference as a solid black line in each panel. Scaled down luminosity functions from 1.4 GHz to 610 MHz by Smolčić et al. (2009a), McAlpine et al. (2013), and Novak et al. (2017) are shown as green pluses, orange pentagons, and blue diamonds, respectively, in each panel. The solid red lines in each panel corresponds to the median values of the MCMC samples and the shaded regions correspond to the 68 per cent confidence region of the PLE fit (skyblue) and also the combination of PDE and PLE fitting (grey) to the samples. The redshift range and the median redshift are shown in each panel. The error bars are determined using the prescription of Gehrels (1986).
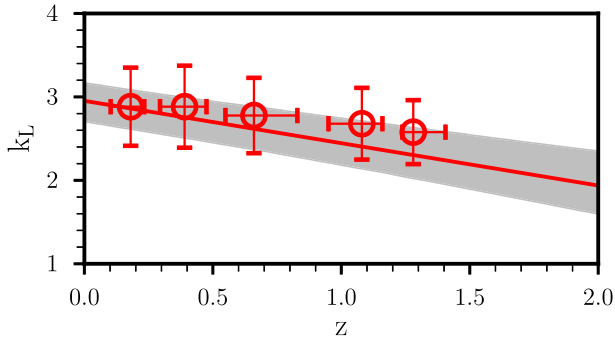
Figure 8. Parameters obtained from fitting PLE model to the SFG luminosity functions. The open red circles show the evolution parameters obtained from fitting the assumed analytic form of the luminosity function in five redshift bins assuming pure luminosity evolution scenario (see the text for details). The vertical error bars represent the median absolute deviation (MAD) of the MCMC samples. The horizontal error bars denote the interquartile range of reshift in each bin. The same colour line shows the results from the continuous fit assuming that the PLE parameter evolves linearly with redshift.

the radio sources is fixed and undergoes PDE parametrized by

$$\Phi_z(L) = (1+z)^{k_D} \Phi_o(L) \tag{9}$$

and another in which the number density of radio sources is fixed and the population undergoes pure luminosity evolution:

$$\Phi_z(L) = \Phi_o\left(\frac{L}{(1+z)^{k_L}}\right), \tag{10}$$

where $\Phi_z(L)$ is the LF at redshift z, $\Phi_o(L)$ the normalization of the local LF, and k_D and k_L represent pure density and pure luminosity evolution parameters, respectively, and denote the strength of the evolution. Both the PLE and PDE models are common in the literature (e.g. see Condon 1984; Sadler et al. 2002, 2007; Gruppioni et al. 2013; McAlpine et al. 2013). Studies have shown that true evolution might be a combination of both of these extremes (see e.g. Yuan, Han & Wen 2016, 2017; Novak et al. 2017). The best-fitting evolution parameters for each redshift bin obtained with this procedure are presented in Table 5. The LMFIT Python package first does the fitting by performing a non-linear least-squares χ^2 minimization to obtain the best-fitting k_L and k_D parameters. The EMCEE is then implemented to calculate the probability distribution for the parameters. From this, we get the medians of the probability distributions and a 1σ quantile, estimated as half the difference between the 15.8 and 84.2 percentiles.

We also fit a continuous model of the redshift dependence of the evolution parameters by adding a redshift-dependent term to the k_L and k_D parameters in equations (9) and (10) (e.g. see Novak et al. 2017, 2018; Smolčić et al. 2017b; Ceraj et al. 2018). We fit a simple linear redshift-dependent evolution model to all SFG luminosity functions in all redshift bins simultaneously given by

$$\Phi(L, z) = (1+z)^{(k_D+z\beta_D)} \times \Phi_0\left[\frac{L}{(1+z)^{(k_L+z\beta_L)}}\right], \tag{11}$$

where k_D, k_L, β_D, and β_L are the various evolution parameters. Equation (11) considers the case with both density and luminosity evolution combined plus redshift dependence (i.e. four free parameters). We test pure density and pure luminosity evolution together via the procedure described above. The 68 per cent confidence region by combining PDE and PLE fitting to the samples are shown with grey shaded are Fig. 7.
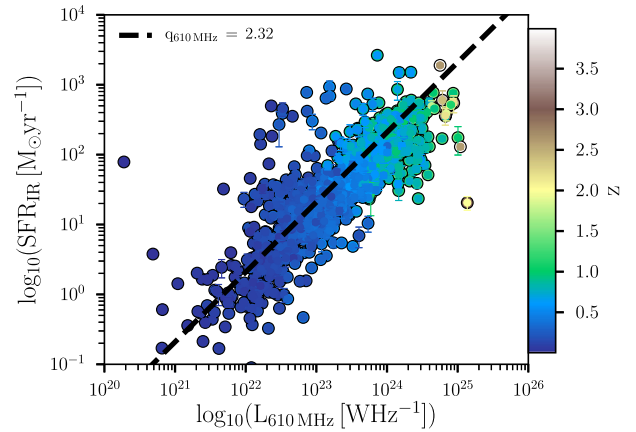
Figure 9. SFR from the total infrared luminosity as a function of radio luminosity at 610 MHz for SFGs. The SFGs are colour coded with redshift. The dotted line shows the SFR, when a non-evolving q-value (i.e. median q-value at 610 MHz in Section 3.1) is assumed.

Fig. 8 presents best-fitting parameters obtained from fitting PLE model to the SFG luminosity functions. The second column of Table 5 presents values of the parameters (i.e. k_L) obtained from fitting PLE model to the SFG luminosity functions. The open red circles show the evolution parameters obtained from independently fitting the assumed analytic form of the luminosity function in five redshift bins assuming pure luminosity evolution scenario whereas the same colour line shows the results from the continuous fit (i.e. jointly fitting the RLF in the five redshift bins) assuming that the PLE parameter evolves linearly with redshift by using equation (11). The vertical error bars represent the median absolute deviation (MAD) (Rousseeuw & Croux 1993) of the MCMC samples. We derive $L_{610\,MHz} \propto (1+z)^{(2.95\pm0.19)-(0.50\pm0.15)z}$ (i.e. $k_L = 2.95 \pm 0.19$) for $0.002 < z < 1.5$. With no uncertainties associated with their estimated value, Haarsma et al. (2000) have found that a PLE with $k_L = 2.74$ is a good representation of the evolution of their radio-selected SF galaxies. Smolčić et al. (2009a) derived 2.1 ± 0.2 or 2.5 ± 0.1 for SFG depending on the choice of the local LF (i.e. Sadler et al. 2002 or Condon 1989 local LFs). Strazzullo et al. (2010) derived $k_L = 2.9 \pm 0.3$ by studying a sample of 1.4 GHz radio sources in the Deep SWIRE Field (DSF), reaching a limiting flux density $\sim 13.5\,\mu$Jy at the centre of a 0.36 deg^2 area. We can therefore compare our results more directly with both Smolčić et al. (2009a) and Strazzullo et al. (2010), keeping in mind that both samples reach only z = 1.3. The evolution we measure is slightly higher than that of Smolčić et al. (2009a) but in good agreement with Strazzullo et al. (2010). However, our value is significantly weaker than found in the IR band for z ≤ 1.3 by Magnelli et al. (2009), who modelled the evolution of infrared luminous SFGs as a PLE and found $k_L = 3.6 \pm 0.4$. McAlpine et al. (2013) studied the evolution of faint radio source out to z ∼ 2.5. They found that the radio population experiences mild positive evolution out to z ∼ 1.2 increasing their space density by a factor of ∼3 with SFGs driving the more rapid evolution at low redshifts, z < 1.2. The McAlpine et al. (2013) translated to 610 MHz are shown in yellow symbols in Fig. 7 and are in good agreement with our values of SFG luminosity functions out to z < 1.5. They reported k_L to be 2.47 ± 0.12 for their radio-selected star-forming population which is consistent with that of Smolčić et al. (2009a) but slightly below our measured value. Padovani et al. (2011) reported the radio power of SFGs evolves

Table 6. Comparison of the current determinations of the evolution of the RLF.

Reference	Field	Wavelength	Redshift	Evolution parameter (PLE)
Hopkins (2004)	-	1.4 GHz	~ 2.0	2.7 ± 0.6
Smolčić et al. (2009a)	COSMOS	1.4 GHz	~ 1.3	2.1 ± 0.2 OR 2.5 ± 0.1
Strazzullo et al. (2010)	DSF	1.4 GHz	~ 1.3	2.9 ± 0.3
Padovani et al. (2011)	CDFS	1.4 GHz	≤ 1.3	$3.5^{0.4}_{-0.7}$
Padovani et al. (2011)	CDFS	1.4 GHz	~ 2.3	$2.89^{+0.10}_{-0.15}$
Novak et al. (2017)	COSMOS	1.4 GHz	~ 5.0	$(3.2 \pm 0.2) - (0.33 \pm 0.08)z$
This work	EN1	610 MHz	~ 1.5	$(2.95 \pm 0.19) - (0.50 \pm 0.14)z$

Notes. COSMOS – Cosmological Evolution Survey.
CDFS – Chandra Deep Field South.
DSF – Deep SWIRE Field.

as $(1 + z)^{2.5-2.9}$ up to $z \leq 2.3$, their maximum redshift in their sample, which in agreement with previous determinations in the radio, IR bands, and this work. Although they also reported the evolution to be $k_L = 3.5^{+0.4}_{-0.7}$ for $z \leq 1.3$ or $k_L = 3.1^{+0.8}_{-1.0}$, when they exclude two large-scale structures in their sample. Novak et al. (2017) presented a radio-selected sample of SFGs from deep VLA-COSMOS 3 GHz observations (Smolčić et al. 2017b) identifying 6040 galaxies, where the radio emission is not dominated by an AGN. Using this sample they derived radio LFs up to $z \sim 5$. The blue diamonds in Fig. 7 show the Novak et al. (2017) LFs scaled down to 610 MHz. Their results are in agreement with our luminosity functions, with their LF constraining the high-luminosity end. By comparing their results with LFs derived using IR- and UV-selected samples and checking their robustness, they reported that their radio LF can be well described by a local LF evolved only in luminosity as $L_{1.4GHz} \propto (1 + z)^{(3.2\pm0.2)-(0.33\pm0.08)z}$. These previous studies are broadly consistent with our radio-derived PLE parameter and Table 6 presents a summary of the comparison.

6 THE COSMIC STAR FORMATION HISTORY TRACED BY THE LOW-FREQUENCY SFG POPULATION

The relationship between the FIR luminosity and the SFR is complex since stars with a variety of ages can contribute to the dust heating, and only a fraction of the bolometric luminosity of the young stellar population is absorbed by dust (e.g. see Lonsdale Persson & Helou 1987; Walterbos & Greenawalt 1996). By adopting the mean luminosity for 10–100 Myr continuous bursts, solar abundances, the Salpeter (1955) initial mass function (IMF) and assuming that the dust reradiates all of the bolometric luminosity yields:

$$\left(\frac{\text{SFR}_{\text{IR}}}{\text{M}_\odot \text{ yr}^{-1}}\right) = \left(\frac{L_{\text{IR}}}{5.8 \times 10^9 \text{ L}_\odot}\right) \tag{12}$$

(see Kennicutt 1998; Bell 2003; Murphy et al. 2011b). To compute the SFRs, we use the redshift-dependent $q_{\text{IR}}(z)$ parameter. This should account for these intrinsic observational limitations under the assumption of a linear IRRC given by

$$\left(\frac{\text{SFR}_{610\text{MHz}(z)}}{\text{M}_\odot \text{ yr}^{-1}}\right) = \mathcal{F}_{\text{IMF}} \times 10^{-24} \, 10^{q_{\text{IR}}(z)} \left(\frac{L_{610\text{MHz}}}{\text{WHz}^{-1}}\right), \tag{13}$$

where $\mathcal{F}_{\text{IMF}} = 1$ for a Chabrier (2003) IMF and $\mathcal{F}_{\text{IMF}} = 1.7$ for a Salpeter (1955) IMF. Novak et al. (2017) stress that since low-mass stars do not contribute significantly to the total light of the galaxy, only the mass-to-light ratio is changed when the IMF adopted is
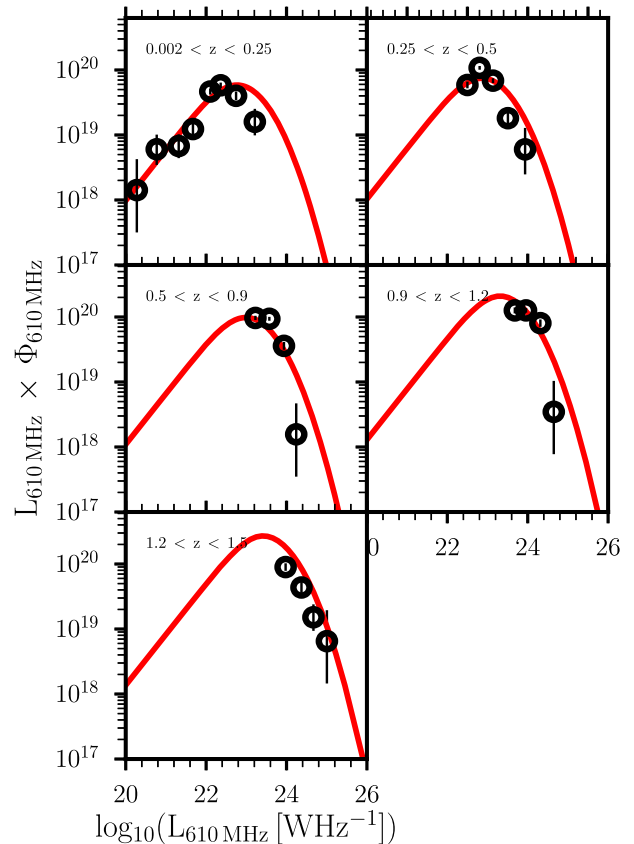
Figure 10. Luminosity density for 610 MHz GMRT SFGs (open black circles) in five redshift bins. The solid red curves correspond to the best-fitting PLE LFs in each redshift bin.

Chabrier (2003). We followed Novak et al. (2017) and used the Chabrier (2003) IMF.

In Fig. 9, we show SFR from the total infrared luminosity as a function of radio luminosity at 610 MHz for SFGs. We colour code the SFGs with redshift and the dotted line shows the SFR, when a non-evolving q-value (i.e. median q-value in Section 3.1) is assumed. Converting the radio luminosity to SFR as shown in equation (12) to equation (13), before performing the integration will yield the star formation rate density (SFRD) of a given epoch as shown in equation (14) below, as presented as well by Novak
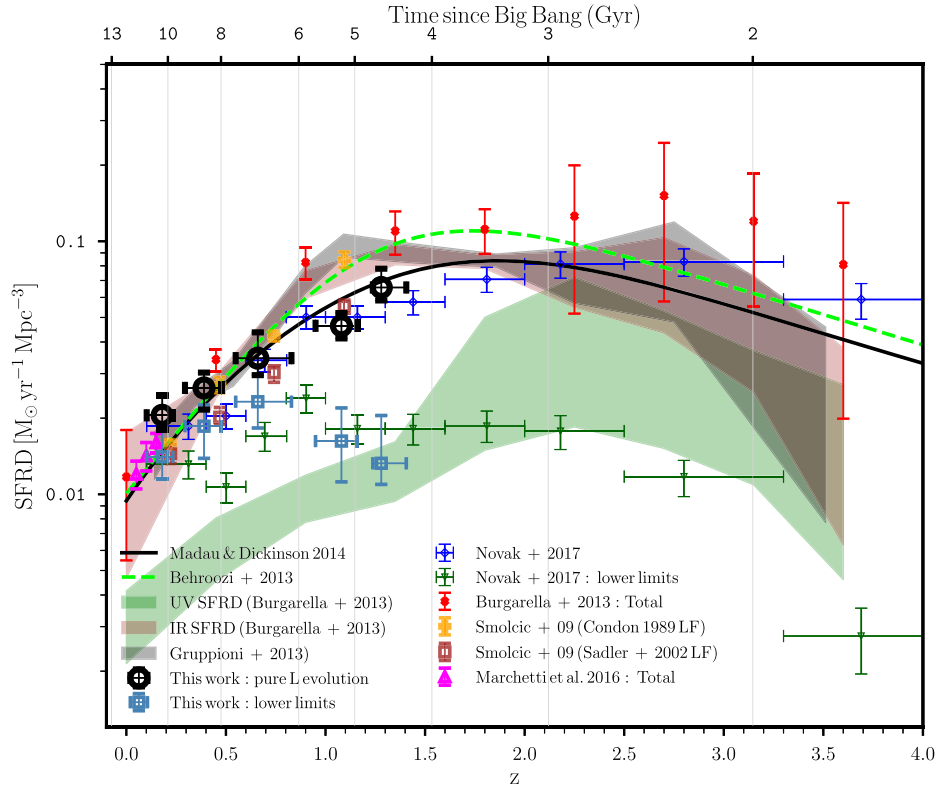
Figure 11. Cosmic SFRD history. Our total SFRD values estimated from the pure luminosity evolution in separate redshift bins are shown as open black circles. See the text for details of the data points shown for comparison that are indicated in the legend. We limit the plot between $0 < z < 4$ redshift range.

et al. (2017)

$$\mathcal{SFRD} = \int_{L_{min}}^{L_{max}} \Phi_{(L,z,k_L,k_D)} \times \text{SFR}(L) \, d(\log L_{610\,\text{MHz}}). \quad (14)$$

To derive the SFR density, we need to compute the radio luminosity density and to convert our radio luminosities into SFRs, in Fig. 10, we show the luminosity density for our five redshift bins. The curves are the PLE (solid red) best fit to the 610 MHz data in each redshift bin. We numerically integrated the expression in equation (14) by taking the analytical form of the LF in each redshift bin and using the best-fitting evolution parameters shown in Fig. 7. We integrated over the entire luminosity range by setting $L_{min} = 0$ and $L_{max} = +\infty$. This ensures that the integral converges and that the major contribution to the SFRD arises from galaxies with luminosities around the turnover of the LF. From this approach, Novak et al. (2017) stress that the entire radio emission is recovered and if the LF shape and evolution is well constrained, the SFRD estimate will be within the SFR calibration errors. We also performed the integration using the data constrained limits, where L_{min} and L_{max} correspond to the lowest and the highest value of the observed LF. This ensures that any bias due to LF extrapolation towards higher or lower luminosities is removed (see Novak et al. 2017). We show our total SFRD derived by integrating the pure luminosity evolved LF in individual redshift bins as open black circles in Fig. 11. Table 5 presents the best-fitting evolution parameters obtained by the fitting local luminosity function to the redshift binned data assuming pure luminosity k_L evolution and the SFRD derived (third column). We compare our SFRD results with other radio-based estimates in Fig. 11. Smolčić et al. (2009a) derived the CSFH out to $z = 1.3$ using the local 20 cm LFs (Condon 1989; Sadler et al. 2002), purely evolved in luminosity, and best fit

to the VLA-COSMOS data in four redshift bins (see yellow pluses and brown squares). SFRD obtained when L_{min} and L_{max} are data-constrained limits (lower limits) are also shown (see light blue squares). Lower limits obtained by Novak et al. (2017) are shown as green triangles. To create a consistent multiwavelength picture, we also compare our work with results in the literature derived at infrared (IR) and UV wavelengths in Fig. 11. All SFR estimates were rescaled to a Chabrier IMF where necessary. The curve from the review by Madau & Dickinson (2014), who performed a fit on a collection of previously published UV and IR SFRD data is shown as a solid black curve. The curve from Behroozi, Wechsler & Conroy (2013) who provide new fitting formulae for star formation histories based on a wide variety of observations is shown as dashed green curve is also shown. The constained SFRD by Burgarella et al. (2013) taking into account dust obscuration using combined IR and UV LFs reported in Gruppioni et al. (2013) and Cucciati et al. (2012), respectively, are shown as red crosses for the total SFRD, red shaded area for the IR SFRD, and green shaded area for the UV SFRD. The grey shaded area denotes the 1σ uncertainty for the SFRD derived from integrated total IR LF by Gruppioni et al. (2013). SFRD estimates including the unobscured contribution based on the UV dust-uncorrected emission from local galaxies by Marchetti et al. (2015) are shown as magenta triangles. The expected steep decline in the SFRD since $z \sim 1$ seen by Smolčić et al. (2009a) and other previous studies is reproduced by our sample.

7 CONCLUSIONS

Over the last few years Bonzini et al. (2013), Padovani et al. (2015), and Smolčić et al. (2017a) have for the first time managed to carry out a complete census of populations contributing to the

faint radio sky at 1.4 and 3.0 GHz with the JVLA. These were done over a relatively small (0.5 and 2 deg^2 for JVLA-ECDFS and JVLA-COSMOS, respectively) contiguous area reaching rms sensitivities (i.e. 6 and 2.3 μJy at 1.4 and 3.0 GHz, respectively) comparable to our study. Such data sets that provide images of the radio flux density over small regions at these sensitivities are still rare but will be achieved by the MeerKAT and SKA1 albeit over much larger areas. We study a sample of 1685 SFGs covering ∼1.86 deg^2 down to a minimum noise of ∼7.1 μJy beam^{-1} in the EN1 field at 610 MHz with the GMRT. The depth of our 610 MHz data represents a potentially very useful tool to address the role of SFGs in galaxy evolution. These SFGs were obtained from a combination of diagnostics from the radio and X-ray luminosity, optical spectroscopy, mid-infrared colours, and 24 μm and IR-to-radio flux ratios. Of the 1685 SFGs from our sample, 496 have spectroscopic redshifts whereas 1189 have photometric redshifts. Deep multiwavelength spectrophotometric data sets with comparable resolutions and sensitivities to our radio data will be needed to improve our source classification. More specifically, mid-infrared multiband photometry and optical/NIR spectroscopy are the limiting factor in our case. However, since deep (wide-area) mid-infrared will not be carried out in the foreseeable future, the best avenue towards improving the diagnostics for such scientific work in the future is via multi-object wide-field optical/NIR spectroscopy.

We study the IRRC for the SFGs. We measure an evolution with redshift of the IRRC for 1.4 GHz radio luminosities to be $q_{IR} = 2.86 \pm 0.04(1 + z)^{-0.20\pm0.02}$, where q$_{IR}$ is the ratio between the total infrared luminosity (L_{IR}, $8-1000$ μm) and the 1.4 GHz radio luminosity ($L_{1.4}$ GHz).

We have used the non-parametric V/Vmax test and the RLF to investigate the cosmic evolution of SFGs. Sadler et al. (2007) found evidence that low-luminosity radio sources experience mild evolution with an increase in their number density by a factor of ∼ 2 at $z = 0.55$. Smolčić et al. (2009a) found a mild evolution of the low-power AGNs in the VLA-COSMOS survey out to $z \sim 1.3$. We construct the RLF at 610 MHz for our SFGs and find positive evolution. This is consistent with previous studies, for the SFG RLF scaled to 610 MHz from 1.4 GHz assuming a spectral index of $\alpha = -0.8$. The exact shape of the radio spectral energy distribution (SED) of SFGs is usually assumed to be a superposition of the steep synchrotron spectrum, described by a power law (see Condon 1992), even so, there are processes which can alter the shape of the spectra. Recent work by Lacki (2013) and Tisanić et al. (2019) has developed theoretical models describing an alternative picture to the simple power-law shape which includes spectral curvature. However, deep multifrequency radio observations of representative samples of galaxies are needed to study the radio SED and understand the physical processes shaping it across redshifts. We also compare our results to models from the literature and find that the Mancuso et al. (2017) and Wilman et al. (2008) models do compare well to our data. However, there is an exception for the lowest redshift bin, where none of the models is able to reproduce the low-luminosity observations. Our LFs behave very well at high luminosities, where other samples (see e.g. Smolčić et al. 2009b) show an excess of sources with respect to models. This can be interpreted as contamination due to AGNs. This can be better addressed with better multiwavelength data and better proven AGN diagnostics. Our radio LFs can be well described by a local LF evolved only in luminosity as $L_{610\,MHz} \propto (1 + z)^{(2.95\pm0.19)-(0.50\pm0.15)z}$.

We converted our radio luminosities to SFRs using a redshift-dependent IRRC. By integrating over the entire luminosity range the LF fits in various redshift bins, we derived the cosmic star formation density out to $z = 1.5$ for our SFG sample. Our estimates

of the SFRD is consistent with previous measurements from the literature when all the SFR estimates are rescaled to a Chabrier IMF. Novak et al. (2017) assumed pure luminosity evolution for their LF, consistent with the measurements by Smolčić et al. (2009b) (and recent result by Gruppioni et al. 2013 assuming the redshift-dependent IRRC parameter). All these studies found broad agreement between the radio SFRD evolution and UV/IR surveys, observing a steep decline from $z = 1$ to 0. Our sample reproduces this expected steep decline in the SFRD since $z \sim 1$. This work represents a benchmark for studying the evolution of the RLF and SFR function with cosmic time at the faint low-frequency regime in spite of our redshift limit.

In the near future, we plan to undertake the exploitation of the MeerKAT International GHz Tiered Extragalactic Exploration (MIGHTEE) Survey (Jarvis et al. 2016) with the MeerkAT SKA precursor (Jonas & MeerKAT Team 2016). MIGHTEE will survey well-studied extragalactic deep fields (E-CDFS, COSMOS, XMM-LSS, and ELAIS-S1), totaling 20 square degrees at 1.4 GHz, to ∼2 μJy beam^{-1} rms. A survey matched in resolution and depth will be undertaken with the upgraded GMRT (Gupta 2014), and this work will thus be precious to make the most of such GMRT data. It is our hope that a complete and expansive review of this topic will be able to do justice to the wealth of current and ongoing measurements contributing to our understanding of this aspect of galaxy evolution. An extensive compilation from the literature of SFR density measurements as a function of redshift will be investigated in future works. This will provide rich compilation of SFR density evolution which will help with a robust constraint for many investigations of galaxy evolution.

REFERENCES

Avni Y., Bahcall J. N., 1980, ApJ, 235, 694
Behroozi P. S., Wechsler R. H., Conroy C., 2013, ApJ, 770, 57
Bell E. F., 2003, ApJ, 586, 794
Bell E. F., Zheng X. Z., Papovich C., Borch A., Wolf C., Meisenheimer K., 2007, ApJ, 663, 834
Best P. N., Kauffmann G., Heckman T. M., Brinchmann J., Charlot S., Ivezić Ž., White S. D. M., 2005, MNRAS, 362, 25
Blanton M. R. et al., 2003, AJ, 125, 2348
Bonaldi A., Bonato M., Galluzzi V., Harrison I., Massardi M., Kay S., De Zotti G., Brown M. L., 2019, MNRAS, 482, 2
Bonzini M., Padovani P., Mainieri V., Kellermann K. I., Miller N., Rosati P., Tozzi P., Vattakunnel S., 2013, MNRAS, 436, 3759
Burgarella D. et al., 2013, A&A, 554, A70
Calistro Rivera G. et al., 2017, MNRAS, 469, 3468
Caputi K. I. et al., 2007, ApJ, 660, 97
Ceraj L. et al., 2018, A&A, 620, A192
Chabrier G., 2003, PASP, 115, 763

Clewley L., Jarvis M. J., 2004, MNRAS, 352, 909
Condon J. J., 1984, ApJ, 287, 461
Condon J. J., 1989, ApJ, 338, 13
Condon J. J., 1992, ARA&A, 30, 575
Condon J. J., Cotton W. D., Broderick J. J., 2002, AJ, 124, 675
Cucciati O. et al., 2012, A&A, 539, A31
de Jong T., Klein U., Wielebinski R., Wunderlich E., 1985, A&A, 147, L6
Delhaize J. et al., 2017, A&A, 602, A4
Dye S., Eales S., Moncelsi L., Pascale E., 2010, MNRAS, 407, L69
Foreman-Mackey D., Hogg D. W., Lang D., Goodman J., 2013, PASP, 125, 306
Gehrels N., 1986, ApJ, 303, 336
Gruppioni C. et al., 2010, A&A, 518, L27
Gruppioni C. et al., 2013, MNRAS, 432, 23
Gupta Y., 2014, Proc. Sci., The Metrewavelength Sky. ASI Conference Series, Pune, 2014, Vol. 13. p.441
Haarsma D. B., Partridge R. B., Windhorst R. A., Richards E. A., 2000, ApJ, 544, 641
Helou G., Soifer B. T., Rowan-Robinson M., 1985, ApJ, 298, L7
Hopkins A. M., 2004, ApJ, 615, 209
Ivison R. J. et al., 2010, A&A, 518, L31
Jarvis M. et al., 2016, Proc. Sci., The MeerKAT International GHz Tiered Extragalactic Exploration (MIGHTEE) Survey. SISSA, Trieste, PoS(MeerKAT2016)006
Jonas J. MeerKAT Team, 2016, Proc. Sci., The MeerKAT Radio Telescope. SISSA, Trieste, PoS(MeerKAT2016)001
Kennicutt Robert C. J., 1998, ApJ, 498, 541
Lacki B. C., 2013, MNRAS, 431, 3003
Lapi A. et al., 2011, ApJ, 742, 24
Lonsdale Persson C. J., Helou G., 1987, ApJ, 314, 513
Madau P., Dickinson M., 2014, ARA&A, 52, 415
Magnelli B., Elbaz D., Chary R. R., Dickinson M., Le Borgne D., Frayer D. T., Willmer C. N. A., 2009, A&A, 496, 57
Magnelli B. et al., 2010, A&A, 518, L28
Magnelli B., Elbaz D., Chary R. R., Dickinson M., Le Borgne D., Frayer D. T., Willmer C. N. A., 2011, A&A, 528, A35
Magnelli B. et al., 2015, A&A, 573, A45
Małek K. et al., 2018, A&A, 620, A50
Mancuso C., Lapi A., Shi J., Gonzalez-Nuevo J., Aversa R., Danese L., 2016a, ApJ, 823, 128
Mancuso C., Lapi A., Shi J., Cai Z.-Y., Gonzalez-Nuevo J., Béthermin M., Danese L., 2016b, ApJ, 833, 152
Mancuso C. et al., 2017, ApJ, 842, 95
Mao M. Y. et al., 2012, MNRAS, 426, 3334
Marchetti L. et al., 2015, MNRAS, 456, 1999
Mauch T., Sadler E. M., 2007, MNRAS, 375, 931
McAlpine K., Jarvis M. J., 2011, MNRAS, 413, 1054
McAlpine K., Jarvis M. J., Bonfield D. G., 2013, MNRAS, 436, 1084
McCarthy P. J. et al., 2001, ApJ, 560, L131
Merloni A., Heinz S., 2007, MNRAS, 381, 589
Middelberg E. et al., 2008, AJ, 136, 519
Mohan N., Rafferty D., 2015, Astrophysics Source Code Library, record ascl:1502.007
Molnár D. C. et al., 2018, MNRAS, 475, 827
Morris S. L., Stocke J. T., Gioia I. M., Schild R. E., Wolter A., Maccacaro T., della Ceca R., 1991, ApJ, 380, 49
Murphy E., Stark A. A., Marrone D., McIntyre V., Vieira J., Carlstrom J., Chapman S., Malkan M., 2011a, Radio spectral indices and accurate positions for high redshift strongly lensed dusty starforming galaxies discovered with the South Pole Telescope, ATNF Proposal
Murphy E. J. et al., 2011b, ApJ, 737, 67
Newville M., Stensitzki T., Allen D. B., Ingargiola A., 2014, LMFIT: Non-Linear Least-Square Minimization and Curve-Fitting for Python, https://zenodo.org/record/11813
Norris R. P. et al., 2006, AJ, 132, 2409
Novak M. et al., 2017, A&A, 602, A5
Novak M., Smolčić V., Schinnerer E., Zamorani G., Delvecchio I., Bondi M., Delhaize J., 2018, A&A, 614, A47

Ocran E. F., Taylor A. R., Vaccari M., Green D. A., 2017, MNRAS, 468, 1156
Ocran E. F., Taylor A. R., Vaccari M., Ishwara-Chandra C. H., Prandoni I., 2019, MNRAS, 491, 1127
Padovani P., Miller N., Kellermann K. I., Mainieri V., Rosati P., Tozzi P., 2011, ApJ, 740, 20
Padovani P., Bonzini M., Kellermann K. I., Miller N., Mainieri V., Tozzi P., 2015, MNRAS, 452, 1263
Pei Y. C., Fall S. M., Hauser M. G., 1999, ApJ, 522, 604
Pilbratt G. L. et al., 2010, A&A, 518, L1
Prandoni I., Guglielmino G., Morganti R., Vaccari M., Maini A., Röttgering H. J. A., Jarvis M. J., Garrett M. A., 2018, MNRAS, 481, 4548
Prescott M. et al., 2016, MNRAS, 457, 730
Rousseeuw P. J., Croux C., 1993, J. Am. Stat. Assoc., 88, 1273
Rowan-Robinson M., 1968, MNRAS, 138, 445
Rowan-Robinson M., Gonzalez-Solares E., Vaccari M., Marchetti L., 2013, MNRAS, 428, 1958
Rujopakarn W. et al., 2010, ApJ, 718, 1171
Sadler E. M. et al., 2002, MNRAS, 329, 227
Sadler E. M. et al., 2007, MNRAS, 381, 211
Salpeter E. E., 1955, ApJ, 121, 161
Sargent M. T. et al., 2010, ApJ, 714, L190
Saunders W., Rowan-Robinson M., Lawrence A., Efstathiou G., Kaiser N., Ellis R. S., Frenk C. S., 1990, MNRAS, 242, 318
Schmidt M., 1968, ApJ, 151, 393
Schmitt J. H. M. M., Kahabka P., Stauffer J., Piters A. J. M., 1993, A&A, 277, 114
Shirley R. et al., 2019, MNRAS, 490, 634
Smolčić V. et al., 2009a, ApJ, 690, 610
Smolčić V. et al., 2009b, ApJ, 696, 24
Smolčić V. et al., 2017a, A&A, 602, A1
Smolčić V. et al., 2017b, A&A, 602, A6
Somerville R. S., Primack J. R., Faber S. M., 2001, MNRAS, 320, 504
Strazzullo V., Pannella M., Owen F. N., Bender R., Morrison G. E., Wang W.-H., Shupe D. L., 2010, ApJ, 714, 1305
Swinbank A. M. et al., 2007, MNRAS, 379, 1343
Tanaka M. et al., 2018, PASJ, 70, S9
Tasse C., Le Borgne D., Röttgering H., Best P. N., Pierre M., Rocca-Volmerange B., 2008, A&A, 490, 879
Thomson A. P. et al., 2014, MNRAS, 442, 577
Tisanić K. et al., 2019, A&A, 621, A139
Vaccari M., 2015, Proc. Sci, The Many Facets of Extragalactic Radio Surveys: Towards New Scientific Challenges. SISSA, Trieste, PoS#27
Vaccari M., 2016, Proc. Sci., The Many Facets of Extragalactic Radio Surveys: Towards New Scientific Challenges (EXTRA-RADSUR2015). SISSA, Trieste, PoS#27
Vaccari M. et al., 2010, A&A, 518, L20
van der Kruit P. C., 1971, A&A, 15, 110
Walterbos R. A. M., Greenawalt B., 1996, ApJ, 460, 696
Willott C. J., Rawlings S., Blundell K. M., Lacy M., Eales S. A., 2001, MNRAS, 322, 536
Wilman R. J. et al., 2008, MNRAS, 388, 1335
Yuan Z. S., Han J. L., Wen Z. L., 2016a, MNRAS, 460, 3669
Yuan Z., Wang J., Zhou M., Qin L., Mao J., 2017, ApJ, 846, 78
Yun M. S., Reddy N. A., Condon J. J., 2001, ApJ, 554, 803
Zheng X. Z., Bell E. F., Rix H.-W., Papovich C., Le Floc'h E., Rieke G. H., Pérez-González P. G., 2006, ApJ, 640, 784

APPENDIX A: LF

The LFs obtained from the $\frac{1}{V_{\max}}$ method for SFGs for the entire redshift range we consider (i.e. $0.002 < z < 1.5$) is shown in Fig. A1 as open black circles. The local RLF from Mauch & Sadler (2007) is represented as black solid line in this figure for comparison. The total SFG RLF for our sample is higher than the SFG RLF of Mauch & Sadler (2007) scaled to 610 MHz assuming $\alpha = -0.8$. This is evident especially at the high-luminosity end and can be attributed to cosmic evolution of the SFGs known to
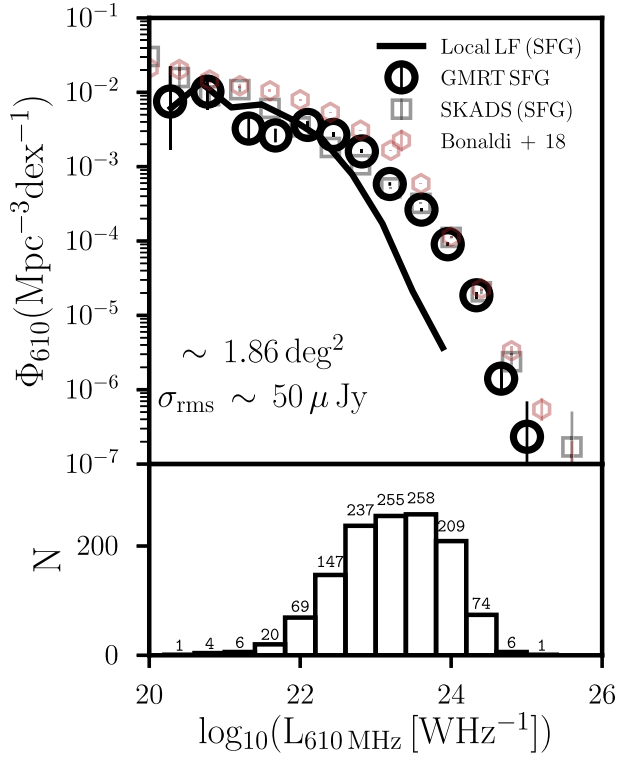
Figure A1. The 610 MHz RLF for SFGs in the redshift range $0.002 < z < 1.5$ is shown in the open black circles. The local RLF of Mauch & Sadler (2007), which has been converted to 610 MHz from 1.4 GHz assuming a spectral index of $\alpha = -0.8$, is shown in the black line. The LF's computed for SFGs from T-RECS (Bonaldi et al. 2019) simulations are shown as open brown diamonds. The error bars are determined using the prescription of Gehrels (1986). The lower panel shows the luminosity distribution with the number of sources in each bin indicated on the bar.

Table A1. 610 MHz RLF for SFGs from $0.002 < z < 1.5$.

Luminosity $\log_{10}(L_{610\,MHz}\,[\mathrm{WHz}^{-1}])$	Number density $\Phi_{610}(\mathrm{Mpc}^{-3}\,\mathrm{dex}^{-1})$	Number
20.28	$7.51^{+14.64}_{-5.70} \times 10^{-3}$	1
20.77	$1.02^{+6.67}_{-3.34} \times 10^{-2}$	4
21.32	$3.25^{+2.61}_{-1.52} \times 10^{-3}$	6
21.67	$2.63^{+0.50}_{-0.54} \times 10^{-3}$	20
22.09	$3.64^{+0.28}_{-0.24} \times 10^{-3}$	69
22.44	$2.67^{+0.17}_{-0.15} \times 10^{-3}$	147
22.82	$1.60^{+0.68}_{-0.63} \times 10^{-3}$	237
23.19	$5.85^{+0.27}_{-0.25} \times 10^{-4}$	255
23.61	$2.64^{+0.09}_{-0.09} \times 10^{-4}$	258
23.95	$9.04^{+0.42}_{-0.39} \times 10^{-5}$	209
24.33	$1.86^{+0.18}_{-0.16} \times 10^{-5}$	74
24.66	$1.41^{+5.10}_{-2.63} \times 10^{-6}$	6
25.00	$2.33^{+5.10}_{-2.63} \times 10^{-7}$	1

Note. The listed luminosity values represent the median luminosity of the sources in the corresponding luminosity bin.

positively evolve with redshift (Mao et al. 2012). Also, this may be attributed to the sensitivity of our radio observations which allows us to probe the source population up to high redshifts. The open brown diamonds show LF's computed for SFGs from T-RECS (Bonaldi et al. 2019) simulations. The faded black squares are RLF computed from the semi-empirical simulation of the SKA (Wilman et al. 2008). This is in good agreement with the RLF we compute for the SFG sample over the same redshift range. The breakdown of the results obtained for the 610 MHz RLF for SFGs from $0.002 < z < 1.5$ is presented in Table A1.

This paper has been typeset from a TeX/LaTeX file prepared by the author.